5-2000

Bending Instability of Electrically Charged Liquid Jets of Polymer Solutions in Electrospinning

Darrell Hyson Reneker
University of Akron Main Campus, reneker@uakron.edu

Alexander L. Yarin

Hao Fong

Sureeporn Koombhongse

Bending instability of electrically charged liquid jets of polymer solutions in electrospinning

Darrell H. Reneker[a)]
Department of Polymer Science, The University of Akron, Akron, Ohio 44325-3909

Alexander L. Yarin
Technion-Israel Institute of Technology, Haifa 32000, Israel

Hao Fong and Sureeporn Koombhongse
Department of Polymer Science, The University of Akron, Akron, Ohio 44325-3909

(Received 20 September 1999; accepted for publication 25 January 2000)

Nanofibers of polymers were electrospun by creating an electrically charged jet of polymer solution at a pendent droplet. After the jet flowed away from the droplet in a nearly straight line, it bent into a complex path and other changes in shape occurred, during which electrical forces stretched and thinned it by very large ratios. After the solvent evaporated, birefringent nanofibers were left. In this article the reasons for the instability are analyzed and explained using a mathematical model. The rheological complexity of the polymer solution is included, which allows consideration of viscoelastic jets. It is shown that the longitudinal stress caused by the external electric field acting on the charge carried by the jet stabilized the straight jet for some distance. Then a lateral perturbation grew in response to the repulsive forces between adjacent elements of charge carried by the jet. The motion of segments of the jet grew rapidly into an electrically driven bending instability. The three-dimensional paths of continuous jets were calculated, both in the nearly straight region where the instability grew slowly and in the region where the bending dominated the path of the jet. The mathematical model provides a reasonable representation of the experimental data, particularly of the jet paths determined from high speed videographic observations. [S0021-8979(00)03609-4]

I. INTRODUCTION

Electrospinning is a straightforward and cost effective method to produce novel fibers with diameters in the range of from less than 3 nm to over 1 μm, which overlaps contemporary textile fiber technology. Polymer nanofibers are being used, or finding uses, in filtration, protective clothing, biomedical applications including wound dressings, drug delivery systems, the design of solar sails, light sails, and mirrors for use in space, the application of pesticides to plants, as structural elements in artificial organs, and in reinforced composites. Ceramic or carbon nanofibers made from polymeric precursors make it possible to expand the list of possible uses for nanofibers. The electrospinning process easily incorporates particles of materials such as pigments, carbon black particles, and many others into the nanofibers that are produced. Flexible fibers are needed on a scale commensurate with micro- or nanoelectrical, mechanical and optical systems. The use of Coulomb forces to fabricate polymer objects may lead to ways to make such fibers *in situ* for such devices.

Observations and a theoretical model of the electrospinning process are presented in this article. The theory accounts for the nonlinear effects that are characteristic of finite perturbations, as well as for the rheological behavior of viscoelastic liquids. The general reason for the bending instability in electrospinning is discussed. The three-dimensional equations describing the dynamics of the bending of electrospun jets are derived and the calculated behavior is compared with experimental observations of jets.

A. History and patents

Interest in the behavior of thin liquid jets in electric fields dates back to the work of Rayleigh.[1] Later Zeleny[2] studied liquid jets in strong electric fields. Theoretical and experimental activities in this area in the last 30 years were revitalized by several important contributions by Taylor.[3–6] He produced useful experimental evidence, and calculated the conical shape of the protrusion from which a jet sometimes leaves the surface of a liquid. Taylor also made the first attempt to calculate the growth rates of both varicose and bending perturbations of electrified liquid jets in the linear approximation when the perturbations are small. In his theoretical analysis, only inviscid fluids were considered.

The bending instability of thin, highly viscous jets moving in air, with no electrical forces, is a kindred phenomenon to that treated in the present work. The theory of the bending instability of uncharged jets was developed and described by Yarin and co-workers.[7–10]

Electrified jets of polymer solutions were investigated as routes to the manufacture of polymer nanofibers.[11–15] Since 1934, when a U.S. patent on electrospinning was issued to Formhals,[16] over 30 U.S. patents have been issued.

a)Electronic mail: dhr@polymer.uakron.edu

B. Formation of bending instability

During the electrospinning of an aqueous solution of high molecular weight polyethylene oxide, a straight jet was formed, as a consequence of electrical forces, from a conical protrusion, often called a Taylor cone,[3] on the surface of a pendent drop of solution. The electrically charged jet traveled for a few centimeters in a straight line. At the end of this straight segment, a diaphanous shape, also conical, with its vertex at the end of the straight segment, was seen when proper illumination was provided. This cone is the envelope, in space, of the complicated set of paths taken by a jet during the observation time. Images obtained with short exposure times by Baumgarten[11] and by Warner *et al.*[17] indicated that the jet was continuously bending for as far as it could be followed after it entered the envelope cone.

C. Electrical charge

The electrical charges referred to in this article are the excess charges, whose electrical fields at long distances are not canceled by nearby counterions. The common assumption that charge moves instantaneously through a metal is not appropriate for ionic conductivity in a moving fluid. In an uncharged ionic solution, there are the same numbers of positive and negative ions in each volume element of the solution and no external field is created. When an external electric field is applied to the solution, the positive and negative ions in the polymer fluid tend to move in opposite directions. Negative ions are forced toward the positive electrode, and positive ions are forced toward the negative electrode. The difference in the number of positive and negative ions in a particular region is often called the excess charge or, simply, the charge. For example, a volume element of the fluid near the negative electrode will then contain more positive ions than negative ions. The excess charge establishes an electrical field that extends for large distances. Adding a soluble salt, which dissociates into equal numbers of positive and negative ions, increases the electrical conductivity of the solution by increasing the number of ions per unit volume, but cannot increase the excess charge. The higher conductivity may, however, shorten the time required for the excess charge, in the form of ions, to move to a particular region in response to changes in the electrical field, or in the shape of a segment of the jet.

D. Ion mobility

The mobility of ions[18,19] through the polymer solution is around $10^{-6}\,m^2/V\,s$. The value of the electric field, determined by dividing the applied potential by the distance between the surface of the pendent drop and the collector plate, was typically 100 000 V/m. The drift velocity of ions inside the jet is then estimated to be 0.1 m/s. The velocity of the segment at the end of the straight segment of the jet was observed to be about 1 m/s in our experiments and about 5 m/s in the work of Warner *et al.*[17] In many cases it is useful to simplify this by assuming that the ionic charge is fixed in the fluid and moves with the jet.

TABLE I. Symbols employed and their definitions.

Symbol	Definition	Unit (cgs)
a	Cross-section radius	cm
a_0	Initial cross-section radius	cm
e	Charge	$(g^{1/2}\,cm^{3/2})/s$
f_a	Air friction force per unit length	g/s^2
f_g	Gravity force per unit length	g/s^2
G	Elastic modulus	$g/(cm\,s^2)$
h	Distance from pendent drop to grounded collector	cm
L	Length scale, $L=(e^2/\pi a_0^2 G)^{1/2}$	cm
L_z	Length of the straight segment	cm
ℓ	Length of the ideal rectilinear jet	cm
m	Mass	g
t	Time	s
v	Velocity	cm/s
V_0	Voltage	$g^{1/2}\,cm^{1/2}/s$
W	Absolute value of velocity	cm/s
α	Surface tension	g/s^2
ζ	Initial segment length	cm
λ	Perturbation wavelength	cm
μ	Viscosity	$g/(cm\,s)$
ν	Kinematic viscosity	cm^2/s
σ	Stress	$g/(cm\,s^2)$
ρ	Density	g/cm^3
ρ_a	Air density	g/cm^3
θ	Relaxation time$(=\mu/G)$	s
ω	Frequency of the perturbation	s^{-1}

E. Tables of symbols and dimensionless groups

The international system of units [Système International (SI)] was used to report the values of experimental measurements. Gaussian units that are customary in fluid mechanics and electrostatics have been also used, as well as dimensionless combinations of parameters to provide concise coverage of the multidimensional parameter space. The numerical results from the calculations were converted to SI units for comparison with the experimental observations. Table I of symbols and Table II of dimensionless groups of parameters are provided.

F. Outline of the article

In Sec. II the experimental setup is described. Section III contains the results of the experimental observations. In Sec. IV the mathematical model of the phenomenon is given, and the reasons for the jet bending are explained. In Sec. V the theoretical results are presented and compared with the experimental data, and a discussion is also presented. Summary and conclusions of the work are presented in Sec. VI.

II. EXPERIMENT

Figure 1 is a sketch of the experimental apparatus. In this article, words such as up, down, top and bottom are used to simplify the description of the experimental arrangements and the observations. The jet flowed downward from the surface of a pendent drop of fluid toward a collector at a distance h below the droplet. An electrical potential difference, which was around 20 kV, was established between the surface of the liquid drop and the collector. The distance, h,

TABLE II. Dimensionless groups and parameters employed and their definitions.

Symbol	Dimensionless group	Dimensionless parameter	Definition
A	Surface tension		$(\alpha\pi a_0^2\mu^2)/(mL^2G^2)$
H	Distance from pendent drop to grounded collector		h/L
K_s	Perturbation frequency		$\omega\mu/G$
K_t	Perturbation wave number		$2\pi L/\lambda$
Q	Charge		$(e^2\mu^2)/(L^3mG^2)$
V	Voltage		$(eV_0\mu^2)/(hLmG^2)$
F_{ve}	Elastic modulus		$(\pi a_0^2\mu^2)/(mLG)$
$\overline{t}$		Time	$t/(\mu/G)$
$\overline{W}$		Absolute value of velocity	$W/(LG/\mu)$
$\overline{\ell}$		Length of the rectilinear part of the jet	ℓ/L
$\overline{v}$		Velocity	$v/(LG/\mu)$
$\overline{\sigma}$		Stress	σ/G

was around 0.2 m. The nanofibers formed a mat on the collector. The coordinates used in the mathematical description are also shown. A magnified segment of the jet near the top of the envelope cone shows the electrical forces that cause the growth of the bending instability. These forces are described in detail in Sec. IV E and Fig. 12.

In general, the pendent drop may be replaced by other fluid surfaces such as films on a solid or shapes generated by surface tension and flow. The collector is usually a good electric conductor. The charged nanofibers may be collected on an insulator, although a way to neutralize the charge carried by nanofibers must be provided in order to collect many layers of nanofibers. Airborne ions from a corona discharge provide an effective way to neutralize the charge on the jets and on the nanofibers. Nanofibers may also be collected on the surface of a liquid.

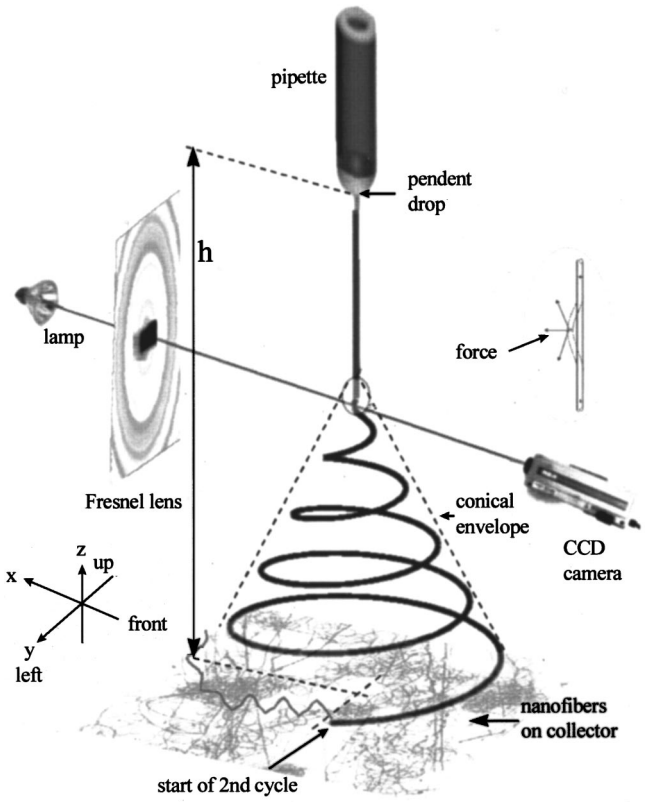

FIG. 1. Schematic drawing of the electrospinning process, showing the jet path, reference axes, relative arrangement of parts of the apparatus at different scales, and the region where the bending instability grew rapidly.

Experiments on electrospinning[15,20] typically use setups similar to that sketched in Fig. 1. All experiments were performed at room temperature, which was about 20 °C. Polyethylene oxide with a molecular weight of 400 000, at a weight concentration of 6%, was dissolved in a mixture of around 60% water and 40% ethanol. Fresher solutions produced jets that traveled further before the first bending instability appeared. The solution was held in a glass pipette with an internal diameter of about 1 mm. At the beginning of the experiment, a pendent droplet of polymer solution was supported at the tip of the capillary. The liquid jet formed on the surface of the pendent drop of solution. When the electrical potential difference (measured in volts, and often referred to as the applied voltage) between the capillary and the grounded collector is increased, the surface of the liquid becomes charged by the electrical field induced migration of ions through the liquid. Instability of the droplet set in when the potential difference was high enough that electrical forces overcame the forces associated with surface tension.[3] Above this threshold, a stable liquid jet emerged. The jet carried away excess ions that migrated to the surface when the potential was applied. A higher potential difference created a higher charge on the jet. For low conductivity solutions, a significant time may be required for the charge to reach a saturation value after the applied potential changes, since charge transport within the fluid is limited by the finite mobility of the ions.

A region about 5 mm across near the vertex of the envelope cone was imaged with a lens that had a focal length of 86 mm and an f number of 1.0. The lens was placed about 20 cm from the jet to avoid disturbing the electrical field near the jet. The image produced by this lens was observed using a 12.5–75 mm, f 1.8 zoom lens on an electronic camera that recorded up to 2000 frames per second with exposure times

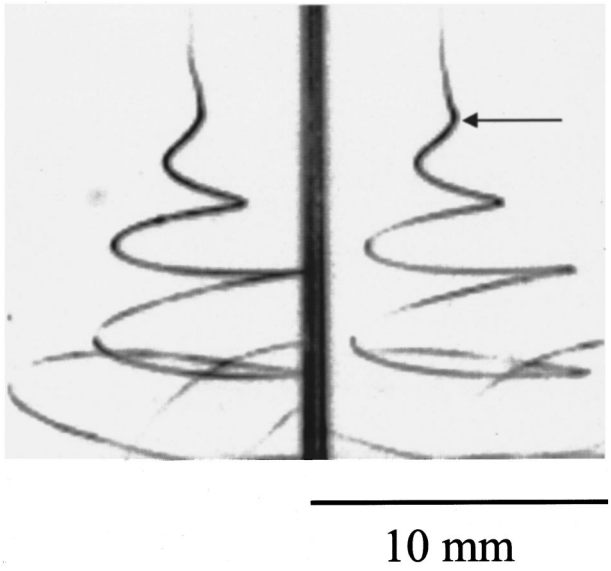

FIG. 2. Stereographic images of an electrically driven bending instability. The exposure time was 0.25 ms. The arrow marks a maximum lateral excursion of a loop.

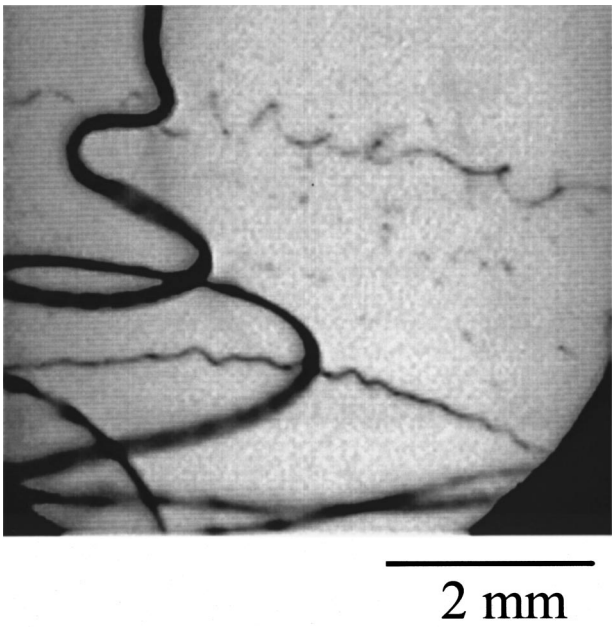

FIG. 3. Image of the end of the straight segment of the jet. The exposure time was 0.25 ms.

as short as 0.0125 ms, although the exposure times used in this work were longer.

The light source was a 50 W halogen lamp with a faceted parabolic reflector. A Fresnel condenser lens was used to project an image of the halogen lamp and its reflector onto the region occupied by the cone. The Fresnel lens had a focal length of 19 cm and a diameter of 30 cm. The central 15 cm diameter part of the Fresnel lens was covered so that the camera received the light scattered from the jet superimposed upon the dark background produced by the covered part of the Fresnel lens.

Images for stereographic viewing were obtained by removing the 86 mm lens, which reduced the magnification so that a region about 1 cm wide is shown in each image in Fig. 2. A pair of wedge prisms that were 40 mm high and 55 mm wide were placed about 20 cm in front of the jet. Each prism deflected the light beam that passed through it by 5°. The zoom lens on the electronic camera, viewing the jet through the two prisms, produced side by side images of the jet from two directions that were 10° apart on each frame that was recorded. These paired images were viewed stereoscopically during playback to produce a slowed down, three-dimensional image of the moving jet. Image processing and analysis was done with Adobe Photoshop, Corell Photopaint and the software supplied with the electronic camera.

III. OBSERVATIONS

A. Jet paths

The region near the vertex of the envelope cone was imaged at 2000 frames per second. These images showed the time evolution of the shape of the jet clearly and in detail. Stereographic images such as those in Fig. 2 showed the shape in three dimensions. The expanding spiral in Fig. 2 is a simple example of the kinds of paths that were observed. After a short sequence of unstable bending back and forth, with growing amplitude, the jet followed a bending, winding, spiraling and looping path in three dimensions. The jet in each loop grew longer and thinner as the loop diameter and circumference increased. Some jets, which are shown in Figs. 3–5, drifted downwards at a velocity much slower than the downward velocity of the smaller loops close to the vertex of the envelope cone. After some time, segments of a loop suddenly developed a new bending instability, similar to, but at a smaller scale than, the first. Each cycle of bending instability can be described in three steps.

Step (1) A smooth segment that was straight or slightly curved suddenly developed an array of bends.

Step (2) The segment of the jet in each bend elongated and the array of bends became a series of spiraling loops with growing diameters.

Step (3) As the perimeter of the loops increased, the cross-sectional diameter of the jet forming the loop grew smaller; the conditions for step (1) were established on a smaller scale, and the next cycle of bending instability began.

This cycle of instability was observed to repeat at an even smaller scale. It was inferred that more cycles occur, reducing the jet diameter even more and creating nanofibers. After the second cycle, the axis of a particular segment may point in any direction. The fluid jet solidified as it dried and electrospun nanofibers were collected some distance below the envelope cone.

The vector sum of forces from the externally applied field, the charge momentarily held in space by the jet, and air drag caused the charged segments to drift towards the collector. Except for the creation of the pendent droplet, the electrospinning process discussed in this article depends only slightly on the gravity of the Earth.

Figure 3 shows the jet entering in the upper left corner, near the end of the straight segment of a jet, and the vertex of

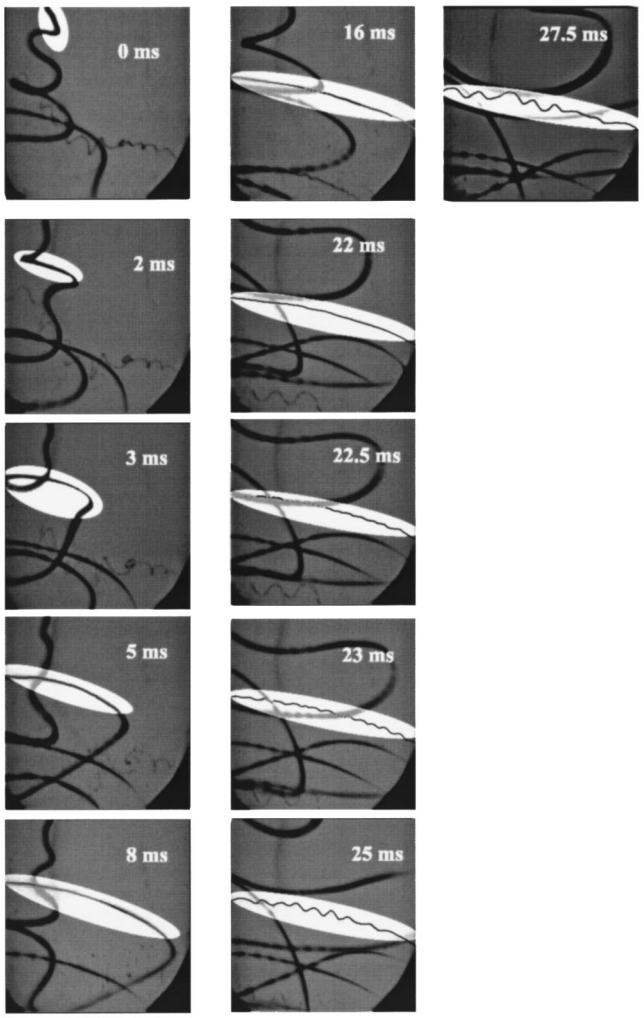

FIG. 4. Evolution of electrical bending instability. The exposure times were 0.25 ms. The width of each image was 5 mm.

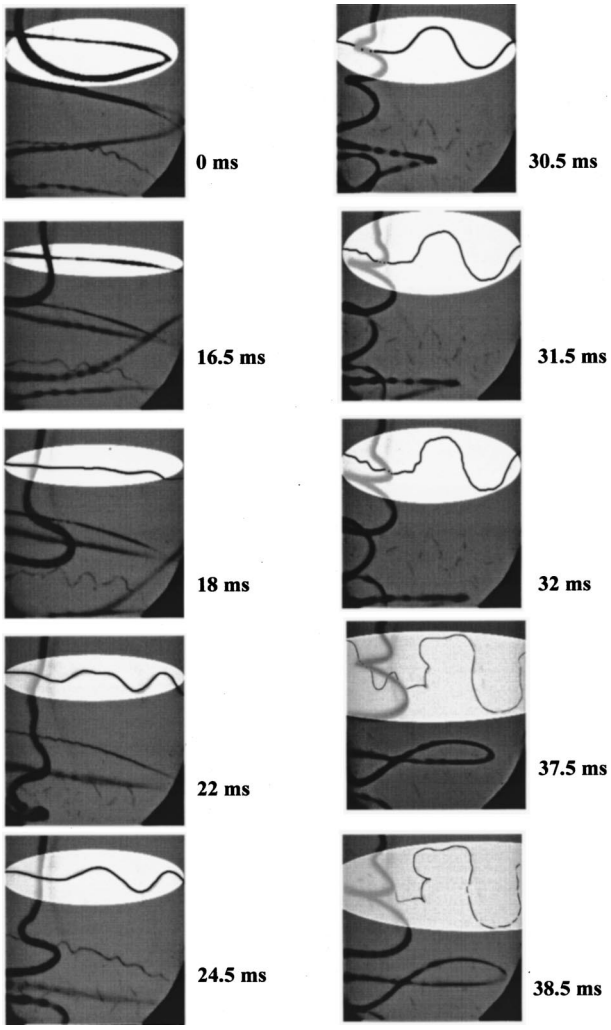

FIG. 5. Images of secondary and tertiary cycles of bending instabilities. The exposure time was 0.25 ms. The width of each image is 5 mm.

the envelope cone, where the first bending instability grew. Several segments of the jet are shown, including segments from slowly moving loops that formed earlier. All these segments are connected by segments that are not shown. Two smooth segments cross each other in this image, as they run nearly horizontally across the bottom of the image. These two segments are noticeably thinner than the jet entering the image because the jet elongated as time evolved. These slowly moving segments were part of large loops and were affected both by air drag and by the disturbance of the applied electrical field caused by the presence of both charged segments of the jet and charged nanofibers below the region being observed. Such slowly moving segments remained in view for many frames.

Two thinner segments that formed even earlier are also included in Fig. 3. One runs across the top half of the image, and the other runs across the bottom half. In the lower of these segments the successive bends (step 1 of the second cycle) were apparent. In the upper segment, the bends had already developed into spiraling loops (step 2 of the second cycle). The pattern of dots visible in the lower left corners of Figs. 3–5 was caused by the pattern of facets on the reflector of the halogen lamp used to illuminate this experiment. These dots are not evidence of the familiar varicose instability that may cause a liquid jet to become a series of droplets. No varicose instability was observed in this experiment.

Using a set of image files created by the electronic camera, it was often possible to follow the evolution of the shape of spiraling segments, such as those shown in Fig. 3, back to the straight segment that entered the upper left corner of the image. In Figs. 4 and 5, the light ellipse in the first image marks a segment that evolved in an interesting way. The selected segment of the jet was followed forward in time, from the moment it entered the region contained in the images until it elongated, looped, became unstable, bent, entered the next cycle, and ultimately became too thin to form an image.

Figure 4 starts with a bend near the end of the straight segment of a jet entering the image at the upper left. The onset of the electrically driven bending instability occurred just before the jet entered the image. The straight segment of the jet extended upward, and is not shown. The segment of the jet that is highlighted by the white ellipse was followed for 27.5 ms in a series of images that were recorded at 0.5 ms intervals. The thinner segments of the jet were emphasized by using the Photopaint 6 software to reproduce them. Places

where the faint image of the jet was ambiguous are indicated by dots, seen, for example, in the image at 22.5 ms.

Eleven images were selected from this series of 55 images to show the evolution of the highlighted segment. The time intervals between the images that are shown vary. Many images that show only a gradual evolution of the path were omitted to simplify Fig. 4. The time at which the first image was captured is taken as time zero. The elapsed time at which each of the following images was recorded is given in Fig. 4.

The looping segment being observed at zero time elongated for 10 ms in Fig. 4. Its further elongation was not followed, because the loop had extended entirely across the image. The rate of increase in the length of the highlighted segment was around 120 mm/s. After 22 ms the visible part of the highlighted segment still appeared in Fig. 4 as a smooth, slightly curved line. In the short time interval between 22.0 and 22.5 ms, this long, slightly curved, smooth segment suddenly became unstable. A linear array of bends appeared, marking the beginning of the second cycle. The lateral amplitude of the bends grew to about 1 mm, and the spatial period of the bends along the segment was also about 1 mm.

These smaller bent segments of the jet continued to elongate, but the images of the trajectories grew fainter and soon were ambiguous. The elongation and the associated thinning presumably continued as long as the charge on the jet supplied enough force. Meanwhile, the elongational viscosity increased as the jet dried. Eventually the jet solidified and the elongation stopped. The evolution of the solidification process remains to be investigated.

The first image in Fig. 5 shows a selected segment that was tracked back to the highlighted area near the bottom of the straight segment. This loop grew in diameter as the jet elongated and became thinner. After 18 ms, an array of bends that had a relatively long wavelength developed. These bends evolved gradually to the path shown at 30.5 ms. Then a tertiary array of bends developed on the highlighted segment during the next 0.5 ms, and quickly evolved to the path shown at 31.5 ms. The growth of the tertiary excursions was followed until 38.5 ms after the first image, at which point the jet was so thin that its image could no longer be followed.

B. Jet splaying

The circled region in Fig. 6 shows a jet that split into two jets that splayed apart, with the axis of the thinner branch generally perpendicular to the axis of the primary jet. The thinner jet disappeared in a few milliseconds, in some cases because it rapidly became even thinner, and in other cases because its path left the field of view. No bending instability was observed on the thinner segment, probably because it was not observed long enough for an instability to develop. Only a few such events were observed in the thousands of images of polyethylene oxide solution examined.

Before the high frame rate, short exposure time images of Figs. 4 and 5 were available, visual observations and video images of electrically driven jets were interpreted as evidence of a process that splayed the primary jet into many smaller jets. The smaller jets were supposed to emerge from the region just below the apex of the envelope cone. Figure 7(a) shows an image from a video frame with an exposure of 16.7 ms. The envelope cone was illuminated with a single bright halogen lamp that projected a narrow beam, through the envelope cone, toward, but not directly into, the lens, so that most of the light that entered the video camera was scattered from the jets.

Figure 7(b) shows a jet similar to that shown in Fig. 7(a) that was illuminated with light from two halogen lamps and

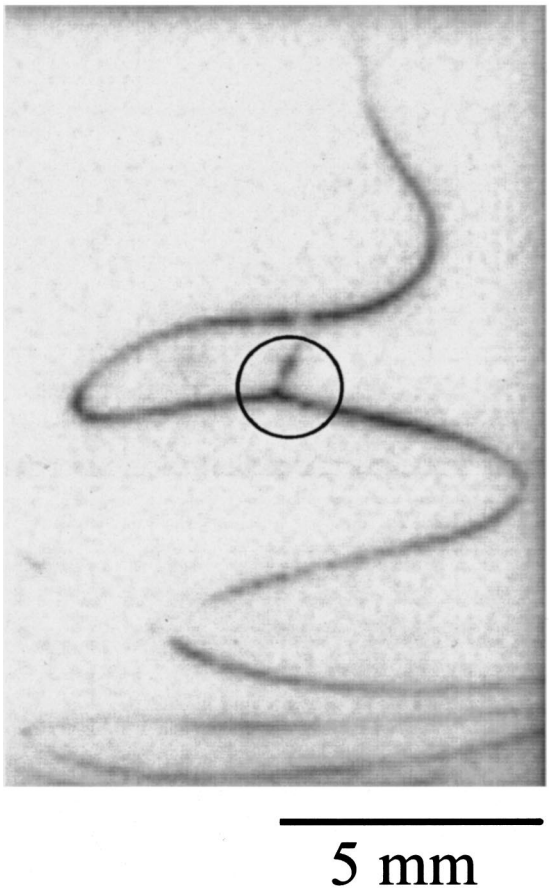

FIG. 6. A jet splits off the primary jet and splays to a different direction.

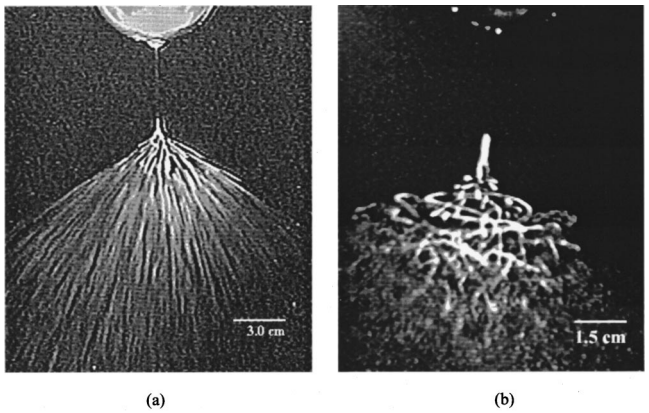

FIG. 7. Images of electrospinning jet with longer camera exposure times: (a) 16.7 and (b) 1.0 ms.

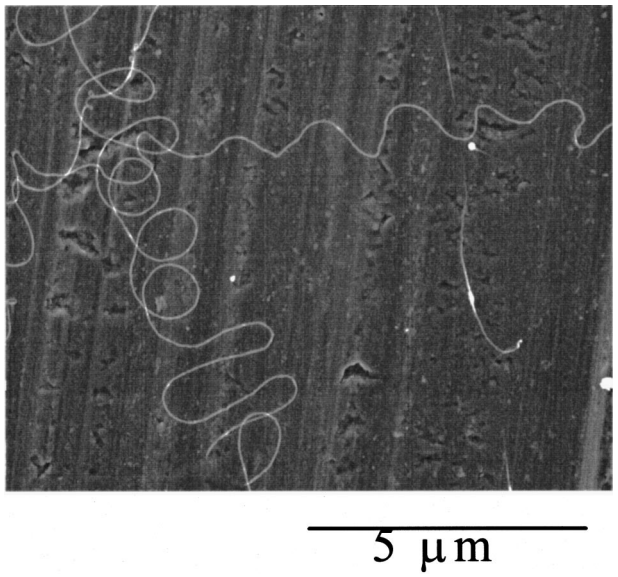

FIG. 8. Scanning electron micrograph of coiled and looped nanofibers on the surface of an aluminum collector.

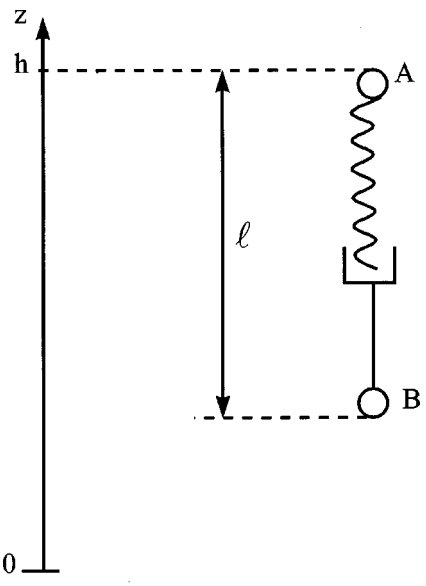

FIG. 9. Viscoelastic dumbbell representing a segment of the rectilinear part of the jet.

photographed with a video camera. The two lamps were above and behind the jet. One was to the left and the other to right. This provided a broader source of illumination than that used for Fig. 7(a), but not as uniform as the Fresnel lens arrangement shown in Fig. 1. An exposure time of 1 ms was used. The part of the straight jet with small bending amplitude is visible as are the loops containing segments, which had turned so that the axis of the segment formed a high angle with the axis of the straight segment. The parts of the jet nearer the vertex of the envelope cone appeared only as short, unconnected lines. Specular reflections of the beam of light, called glints, from one or the other of the two halogen lamps off nearly horizontal segments of downward moving loops were shown to be the cause of these bright spots. Similar bright spots moved downwards during the longer exposure of Fig. 7(a), and created the lines that are prominent in Fig. 7(a).

The video frame rate of 30 frames per second was not fast enough to follow the smooth development of the jet path. At this frame rate, for any particular frame, the preceding and the following frames showed loops and spirals in completely different positions. Only after the illumination was improved, described in Sec. II, and the high frame rate electronic camera used was it obvious that the envelope cone was occupied by one long, flowing, continuous, and ever thinner jet. The repeated cycles of ever smaller electrically driven bending instabilities created a complex path in which the directions of the axes of the connected segments were often different and changing, sometimes by large angles.

C. Coiled and looped jets captured on a hard surface

Nanofibers were sometimes collected by moving a glass microscope slide, a metal screen, or other solid surfaces through the conical envelope. Figure 8 shows that coiled and looped nanofibers collected in this way were similar in shape to the bending instabilities photographed with the high speed camera. The abundance and single coil of the coiled loops depended on the distance below the vertex at which they were collected.

The well-known tendency[9] of a straight liquid jet moving in its axial direction to coil when it impacts a hard, stationary surface and buckles could account for some of the observed coils. This mechanical effect is easily observed when a gravity driven jet of honey falls onto a hard surface. The occurrence of mechanical buckling during impact is likely to be infrequent because most of the long segments of the jet were moving in a sidewise direction as they encountered the collector. It is interesting to hypothesize that in these experiments the coils and loops solidified before collection. Then, the collected coils and loops provide information about the smallest bending instabilities that occurred.

IV. MATHEMATICAL DESCRIPTION OF A JET

A. Viscoelastic model of a rectilinear electrified liquid jet

Consider first a rectilinear electrified liquid jet in an electric field parallel to its axis. We model a segment of the jet by a viscoelastic dumbbell as shown in Fig. 9. In the mathematical description, we use the Gaussian electrostatic system of units. Corresponding SI units are given when parameters are evaluated. Table I lists the symbols and their units.

Each of the beads, A and B, possesses a charge e and mass m. Let the position of bead A be fixed by non-Coulomb forces. The Coulomb repulsive force acting on bead B is $-e^2/\ell^2$. The force applied to B due to the external field is $-eV_0/h$. The dumbbell, AB, models a viscoelastic Maxwellian liquid jet. Therefore the stress, σ, pulling B back to A is given by[21]

$$\frac{d\sigma}{dt} = G\frac{d\ell}{\ell\, dt} - \frac{G}{\mu}\sigma, \tag{1}$$

where t is time, G and μ are the elastic modulus and viscosity, respectively, and ℓ is the filament length. It should be emphasized that according to Refs. 9 and 22, the phenomenological Maxwell model adequately describes rheological behavior of concentrated polymeric systems in strong uniaxial elongation, which is the case in the present work.

The momentum balance for bead B is

$$m\frac{dv}{dt} = -\frac{e^2}{\ell^2} - \frac{eV_0}{h} + \pi a^2 \sigma, \tag{2}$$

where a is the cross-sectional radius of the filament, and v is the velocity of bead B which satisfies the kinematics equation

$$\frac{d\ell}{dt} = -v. \tag{3}$$

B. Introduction of dimensionless parameters

We adopt dimensionless descriptions, as is customary in fluid mechanics[23] (see Table II). We define the length scale $L=(e^2/\pi a_0^2 G)^{1/2}$, where a_0 is the initial cross-sectional radius at $t=0$, and render ℓ dimensionless by L, and assume L to also be an initial filament length which is not restrictive. To make them dimensionless, we divide t by the relaxation time μ/G, stress σ by G, velocity v by LG/μ, and radius a by a_0. Denoting $W=-v$ and applying the condition that the volume of the jet is conserved,

$$\pi a^2 \ell = \pi a_0^2 L, \tag{4}$$

we obtain Eqs. (1)–(3) in the following dimensionless forms:

$$\frac{d\bar{\ell}}{d\bar{t}} = \bar{W}, \tag{5a}$$

$$\frac{d\bar{W}}{d\bar{t}} = V - F_{ve}\frac{\bar{\sigma}}{\bar{\ell}} + \frac{Q}{\bar{\ell}^2}, \tag{5b}$$

$$\frac{d\bar{\sigma}}{d\bar{t}} = \frac{\bar{W}}{\bar{\ell}} - \bar{\sigma}, \tag{5c}$$

where the dimensionless parameters are denoted by bars, and the dimensionless groups are given by

$$Q = \frac{e^2\mu^2}{L^3 m G^2}, \tag{6a}$$

$$V = \frac{eV_0\mu^2}{hLmG^2}, \tag{6b}$$

$$F_{ve} = \frac{\pi a_0^2 \mu^2}{mLG}. \tag{6c}$$

It is emphasized that, in this momentum balance, we temporarily neglect the secondary effects of the surface tension, gravity and the air drag force. Note also that using the definition of L, we obtain from Eqs. (6a) and (6c) that $Q \equiv F_{ve}$. It should also be mentioned that, here in Eq. (4) and hereinafter in this model, we neglect mass losses due to evaporation. In principle, they can be accounted for using a specific expression for the evaporation rate. Evaporation is not expected to introduce qualitative changes in jet dynamics in the main part of the jet path. However, the effect of solvent evaporation on the values of the rheological parameters of the polymer solution, which are not fully known at present, ultimately leads to the solidification of the jet into a polymer fiber.

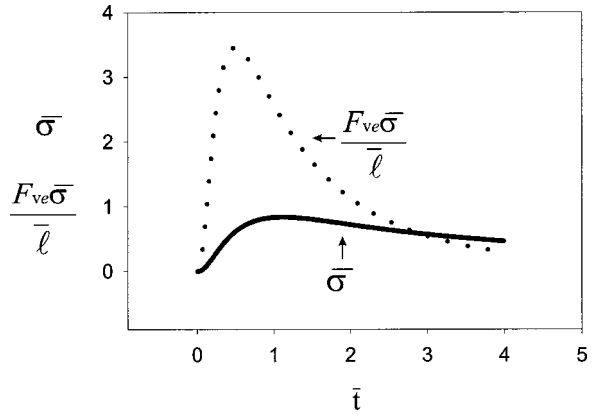

FIG. 10. Longitudinal stress $\bar{\sigma}$ in the rectilinear part of the jet, and the longitudinal force $F_{ve}\bar{\sigma}/\bar{\ell}$. $Q=12$, $V=2$, $F_{ve}=12$.

C. Stress and force along the jet axis

Numerical solutions of the system, Eqs. (5), may be found using the following initial conditions $\bar{t}=0$:

$$\bar{\ell} = 1, \tag{7a}$$

$$\bar{W} = 0, \tag{7b}$$

$$\bar{\sigma} = 0. \tag{7c}$$

Rheological and electrical parameters of the polymer solution are at present not fully known from experiments. Therefore here and hereinafter the calculations were done with the best values available for the dimensionless groups. In certain cases the values were chosen as close as possible to plausible estimates of the physical parameters involved. In these cases we list the values of the physical parameters along with the values of the dimensionless groups based on them. The calculated results in Fig. 10 show that the longitudinal stress $\bar{\sigma}$ first increases over time as the filament stretches, passes a maximum, and then begins to decrease, since the relaxation effects always reduce the stress at long times. The dimensionless longitudinal force in the filament, $F_{ve}\bar{\sigma}/\bar{\ell}$, passes its maximum before $\bar{\sigma}$ does. At the conditions corresponding to the maximum of $\bar{\sigma}$ the value of the force is already comparatively small and decreasing rapidly. We will see below that this small value of the longitudinal force allows the onset of an electrically driven bending instability. Therefore, we identify the filament length, $\bar{\ell}^*$, at the condition when $\bar{\sigma}$ passes the maximum and the longitudinal force is already small, as the length of the rectilinear segment of the electrospun jet at which the bending instability begins to grow rapidly. The relationship of this theoretically defined segment to the observed length of the straight

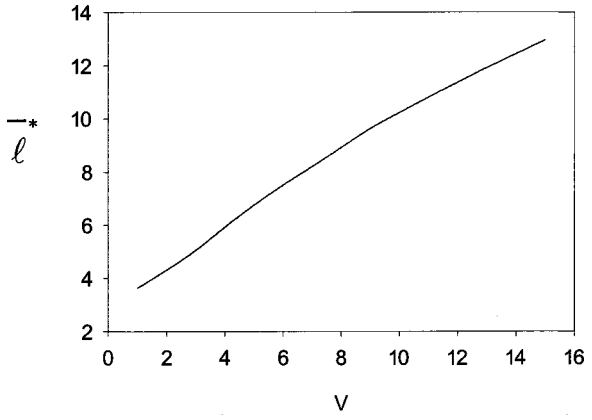

FIG. 11. Length of the rectilinear part of the jet $\bar{\ell}^*$ as a function of the dimensionless voltage V. $Q=12$ and $F_{ve}=12$.

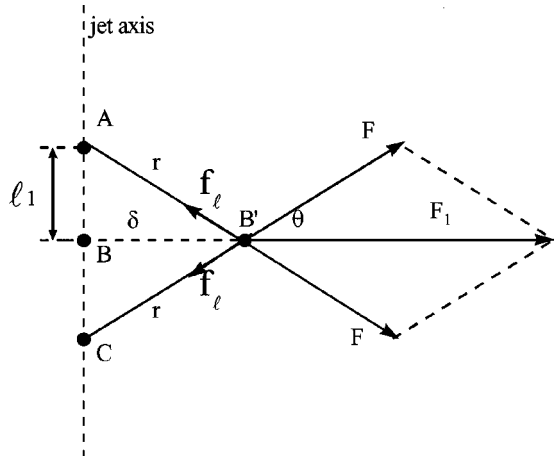

FIG. 12. Illustration of the Earnshaw instability, leading to bending of an electrified jet.

segment is not yet determined. The length, $\bar{\ell}^*$, increases with the applied voltage as is seen in Fig. 11. Near the pendent drop, the longitudinal force is also small, but the jet does not bend, since its radius there is large, and the corresponding bending stiffness is large.

Thin rectilinear liquid jets are unstable to capillary (varicose) perturbations driven by surface tension. Longitudinal stretching can stabilize the jet in the presence of these perturbations.[24] In electrospinning, jets are stretched along their axis by the external electric field and are elongated further by the repulsive force between charges on adjacent segments. The resulting tensile forces prevent development of capillary instability in the experiments reported here.

D. Effects from aerodynamics and gravity are small

For an uncharged jet moving in air at high speed, an aerodynamically driven bending instability may set in if $\rho_a v^2 > \alpha/a$, where ρ_a is the air density, v the jet velocity, and α the surface tension coefficient.[7–9] Taking, for example, $\rho_a = 1.21\,\mathrm{kg/m^3}$, $v \sim 0.5\,\mathrm{m/s}$, $\alpha \sim 0.1\,\mathrm{kg/s^2}$, and $a \sim 10^{-4}\,\mathrm{m}$, we estimate $\rho_a v^2 \sim 0.3\,\mathrm{kg/m\,s^2}$, which is much smaller than $\alpha/a \sim 10^3\,\mathrm{kg/m\,s^2}$. Therefore, under the conditions characteristic of experiments on electrospinning, the aerodynamically driven bending instability does not occur.

The air drag force per unit jet length, which tends to compress the jet along its axis, is given by[25]

$$f_a = \pi a \rho_a v^2 0.65 \left(\frac{2va}{\nu_a}\right)^{-0.81}, \tag{8}$$

where ρ_a and ν_a are the air density and kinematic viscosity, respectively. The gravity force per unit length pulling the jet downward in the experimental geometry shown in Fig. 1 is

$$f_g = \rho g \pi a^2, \tag{9}$$

where ρ is the liquid density and g is the acceleration due to gravity.

In the momentum balance, Eq. (2) or (5b), we neglected f_g as a secondary effect. The air drag force f_a is even smaller than f_g. Taking $\rho_a = 1.21\,\mathrm{kg/m^3}$, $\nu_a = 0.15\times10^{-4}\,\mathrm{m^2/s}$, $\rho = 1000\,\mathrm{kg/m^3}$, $v = 0.5\,\mathrm{m/s}$, and $a = 150\,\mu\mathrm{m}$ we obtain from Eqs. (8) and (9) $f_a = 1.4\times10^{-5}\,\mathrm{kg/s^2}$ and $f_g = 6.9\times10^{-4}\,\mathrm{kg/s^2}$. The compressive stress along the jet axis of the air drag is negligibly small in comparison with the stretching due to gravity, and is much smaller than the stretching due to the electrical forces. Buckling of the electrospun jet due to the compressive force from air drag does not occur, since the electrical forces that tend to elongate the jet are larger and dominate any perturbation that might lead to buckling.

E. Bending instability of electrified jets

The reason for the observed bending instability may be understood in the following way. In the coordinates that move with a rectilinear electrified jet, the electrical charges can be regarded as a static system of charges interacting mainly by Coulomb's law (without the external field). Such systems are known to be unstable according to the Earnshaw's theorem.[26] To illustrate the instability mechanism that is relevant in the electrospinning context, we consider three point-like charges, each with a value e, and originally in a straight line at A, B, and C as shown in Fig. 12. Two Coulomb forces having magnitudes $F = e^2/r^2$ push against charge B from opposite directions. If a perturbation causes point B to move off the line by a distance δ to B', a net force $F_1 = 2F\cos\theta = (2e^2/r^3)\cdot\delta$ acts on charge B in a direction perpendicular to the line, and tends to cause B to move further in the direction of the perturbation away from the line between fixed charges, A and C. The growth of the small bending perturbation that is characterized by δ is governed in the linear approximation by the equation

$$m\frac{d^2\delta}{dt^2} = \frac{2e^2}{\ell_1^3}\delta, \tag{10}$$

where m is the mass.

The growing solution of this equation, $\delta = \delta_0 \exp[(2e^2/m\ell_1^3)^{1/2}t]$, shows that small perturbations increase exponentially. The increase is sustained because electrostatic potential energy of the system depicted in Fig. 12 decreases as e^2/r when the perturbations, characterized by δ

and r, grow. We believe that this mechanism is responsible for the observed bending instability of jets in electrospinning.

If charges A, B, and C are attached to a liquid jet, forces associated with the liquid tend to counteract the instability caused by the Coulomb forces. For very thin liquid jets, the influence of the shearing force related to the bending stiffness can be neglected in comparison with the stabilizing effect of the longitudinal forces since the shearing forces are of the order of $O(a^4)$, which is much smaller than the longitudinal forces,[9] which are of the order of $O(a^2)$. The longitudinal force, at the moment when the bending instability sets in, was calculated above for the stretching of a rectilinear filament. Its value is given by $f_{\ell}=\pi a^2\sigma^*$ (or in dimensionless form by $F_{ve}\overline{\sigma}^*/\overline{\ell}^*$). The values of σ and $\overline{\ell}$ at the moment when σ (or $\overline{\sigma}$) passes its maximum are denoted by asterisks. The forces f_{ℓ} are directed along BC or BA in Fig. 12, and are opposite to the local Coulomb force F. If F is larger than the viscoelastic resistance f_{ℓ}, the bending perturbation continues to grow, but at a rate decelerated by f_{ℓ}.

It might be thought that bending perturbations of very short lengths can always overcome the viscoelastic resistance f_{ℓ}, since the Coulomb force increases when the wavelength of the perturbation decreases. In fact, the surface tension always counteracts the bending instability because bending always leads to an increase of the area of the jet surface.[9] Surface tension resists the development of too large a curvature by the perturbation ABC in Fig. 12, and therefore limits the smallest possible perturbation wavelengths. All these factors are accounted for in the description of the three-dimensional bending instability of electrospun jets in Sec. IV F.

F. Three-dimensional equations of the dynamics of the electrospun jets

We represent the electrospun jets by a model system of beads possessing charge e and mass m connected by viscoelastic elements as shown in Fig. 13, which generalizes the models of Figs. 9 and 12. It needs to be mentioned that these imaginary beads are not the same as the physical beads[20] resulting from the varicose instability. The parameters corresponding to the element connecting bead i with bead $(i+1)$ are denoted by subscript u (up), those for the element connecting bead i with $(i-1)$ by subscript d (down). The lengths ℓ_{ui} and ℓ_{di} of these elements are given by

$$\ell_{ui}=[(x_{i+1}-x_i)^2+(y_{i+1}-y_i)^2+(z_{i+1}-z_i)^2]^{1/2}, \tag{11a}$$

$$\ell_{di}=[(x_i-x_{i-1})^2+(y_i-y_{i-1})^2+(z_i-z_{i-1})^2]^{1/2}, \tag{11b}$$

respectively, where $x_i, y_i, z_i, \ldots$, are the Cartesian coordinates of the beads.

The rates of strain of the elements are given by $(d\ell_{ui}/dt)/\ell_{ui}$ and $(d\ell_{di}/dt)/\ell_{di}$. The viscoelastic forces acting along the elements are similar to Eq. (1),

$$\frac{d\sigma_{ui}}{dt}=G\frac{1}{\ell_{ui}}\frac{d\ell_{ui}}{dt}-\frac{G}{\mu}\sigma_{ui}, \tag{12a}$$

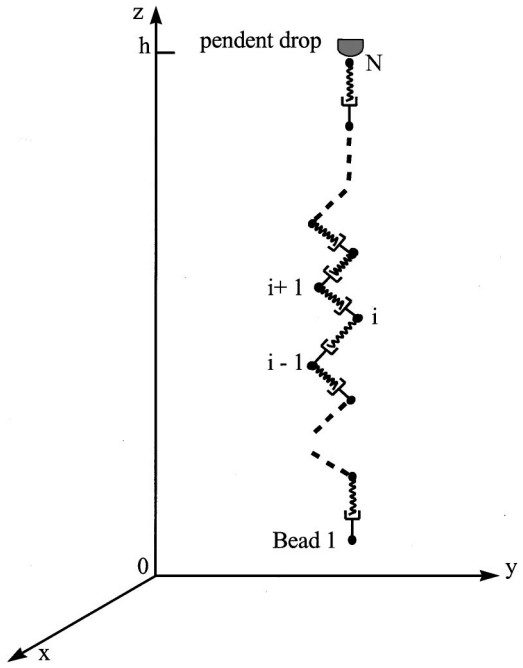

FIG. 13. Bending electrospun jet modeled by a system of beads connected by viscoelastic elements.

$$\frac{d\sigma_{di}}{dt}=G\frac{1}{\ell_{di}}\frac{d\ell_{di}}{dt}-\frac{G}{\mu}\sigma_{di}. \tag{12b}$$

The total number of beads, N, increases over time as new electrically charged beads are inserted at the top of Fig. 13 to represent the flow of solution into the jet. The net Coulomb force acting on the ith bead from all the other beads is given by

$$\mathbf{f}_C=\sum_{\substack{j=1,N\\ j\neq i}}\frac{e^2}{R_{ij}^2}\left[\mathbf{i}\frac{x_i-x_j}{R_{ij}}+\mathbf{j}\frac{y_i-y_j}{R_{ij}}+\mathbf{k}\frac{z_i-z_j}{R_{ij}}\right], \tag{13}$$

where $\mathbf{i}$, $\mathbf{j}$, and $\mathbf{k}$ are the unit vectors along the x, y, and z axes, respectively, and

$$R_{ij}=[(x_i-x_j)^2+(y_i-y_j)^2+(z_i-z_j)^2]^{1/2}. \tag{14}$$

The electric force imposed on the ith bead by the electric field created by the potential difference between the pendent drop and the collector is

$$\mathbf{f}_0=-e\frac{V_0}{h}\mathbf{k}. \tag{15}$$

It is clear that the gravitational force, already shown to be small, may be included in $\mathbf{f}_0$, as is done later in this article to create a hypothetical uncharged jet.

The net viscoelastic force acting on the ith bead of the jet is

$$\mathbf{f}_{ve}=\pi a_{ui}^2\sigma_{ui}\left[\mathbf{i}\frac{x_{i+1}-x_i}{\ell_{ui}}+\mathbf{j}\frac{y_{i+1}-y_i}{\ell_{ui}}+\mathbf{k}\frac{z_{i+1}-z_i}{\ell_{ui}}\right]-\pi a_{di}^2\sigma_{di}\left[\mathbf{i}\frac{x_i-x_{i-1}}{\ell_{di}}+\mathbf{j}\frac{y_i-y_{i-1}}{\ell_{di}}+\mathbf{k}\frac{z_i-z_{i-1}}{\ell_{di}}\right], \tag{16}$$

where, when mass is conserved and evaporation neglected, the filament radii a_{ui} and a_{di} are given by

$$\pi a_{ui}^2 \ell_{ui} = \pi a_0^2 L, \tag{17a}$$

$$\pi a_{di}^2 \ell_{di} = \pi a_0^2 L, \tag{17b}$$

which is similar to Eq. (4).

The surface tension force acting on the ith bead, and tending to restore the rectilinear shape of the bending part of the jet, is given by

$$\mathbf{f}_{\text{cap}} = -\frac{\alpha\pi(a^2)_{av}k_i}{(x_i^2+y_i^2)^{1/2}}[\mathbf{i}|x_i|\text{sign}(x_i)+\mathbf{j}|y_i|\text{sign}(y_i)], \tag{18}$$

where α is the surface tension coefficient, k_i is the jet curvature calculated using the coordinates of beads $(i-1)$, i and $(i+1)$, and $(a^2)_{av}=(a_{ui}+a_{di})^2/4$. The meaning of ''sign'' is as follows:

$$\begin{aligned} &\text{sign}(x)=1, \quad \text{if } x>0,\\ &\text{sign}(x)=-1, \quad \text{if } x<0,\\ &\text{sign}(x)=0, \quad \text{if } x=0. \end{aligned} \tag{19}$$

Setting the forces described in Eqs. (13), (15), (16), and (18) equal to mass times acceleration, according to Newton's second law, we obtain the equation governing the radius vector of the position of the ith bead $\mathbf{r}_i=\mathbf{i}x_i+\mathbf{j}y_i+\mathbf{k}z_i$ in the following form:

$$\begin{aligned} m\frac{d^2\mathbf{r}_i}{dt^2} = &\sum_{\substack{j=1,N\\ j\neq i}}\frac{e^2}{R_{ij}^3}(\mathbf{r}_i-\mathbf{r}_j)-e\frac{V_0}{h}\mathbf{k}+\frac{\pi a_{ui}^2\sigma_{ui}}{\ell_{ui}}(\mathbf{r}_{i+1}-\mathbf{r}_i)\\ &-\frac{\pi a_{di}^2\sigma_{di}}{\ell_{di}}(\mathbf{r}_i-\mathbf{r}_{i-1})-\frac{\alpha\pi(a^2)_{av}k_i}{(x_i^2+y_i^2)^{1/2}}\\ &\times[\mathbf{i}|x_i|\text{sign}(x_i)+\mathbf{j}|y_i|\text{sign}(y_i)]. \end{aligned} \tag{20}$$

For the first bead, $i=1$, and N, the total number of beads, is also 1. As more beads are added, N becomes larger and the first bead $i=1$ remains at the bottom end of the growing jet. For this bead, all the parameters with subscript d should be set equal to zero since there are no beads below $i=1$.

G. Spatial and temporal perturbation of the rectilinear segment

Both space and time dependent perturbations lead to the development of the electrically driven bending instability. To model the way a spatial perturbation develops, we denote the last bead pulled out of the pendent drop and added at the upper end of the jet by $i=N$. When the distance $\ell_{d,N}$ between this bead and the pendent drop becomes long enough, say, $h/25\,000$, a new bead $i=N+1$ is inserted at a small distance, say, $h/50\,000$, from the previous one. At the same time a small perturbation is added to its x and y coordinates,

$$x_i = 10^{-3}L\sin(\omega t), \tag{21a}$$

$$y_i = 10^{-3}L\cos(\omega t). \tag{21b}$$

Here ω is the perturbation frequency. The condition that the collector at $z=0$ is impenetrable is enforced numerically, and the charge on each element of the jet is removed as it arrives at the collector. Such a calculation mimics the development of the electrically driven bending instability. The calculation begins with only two beads, $N=2$. As the jet flows, the number of beads in the jet, N, increases.

It is also possible to consider the temporal instability of an established jet. In this case the calculation began from a long rectilinear filament $0\leqslant z\leqslant h$ containing a fixed number of beads. The filament was perturbed by moving it laterally, at $t=0$, everywhere along its axis by the function

$$x = 10^{-3}L\cos\left(\frac{2\pi}{\lambda}z\right)\frac{h-z}{h}, \tag{22a}$$

$$y = 10^{-3}L\sin\left(\frac{2\pi}{\lambda}z\right)\frac{h-z}{h}, \tag{22b}$$

where λ is the wavelength of the perturbation. Then the temporal evolution of the path was calculated.

In all cases, the system of Eqs. (12) and (20) was solved numerically, assuming that the stresses σ_{ui} and σ_{di} and the radial velocity $d\mathbf{r}_i/dt$ were zero at $t=0$. The equations were made dimensionless by the same scale factors as those in Sec. IV B. Since here it is necessary to account for the surface tension and for the perturbing displacements, three new dimensionless groups emerge in addition to those of Eqs. (6),

$$A = \frac{\alpha\pi a_0^2\mu^2}{mL^2G^2}, \tag{23a}$$

$$K_s = \omega\mu/G, \tag{23b}$$

$$K_t = \frac{2\pi L}{\lambda}. \tag{23c}$$

The last dimensionless group needed is formed by dividing the distance h, from the collector to the pendent droplet, by L,

$$H = \frac{h}{L}. \tag{24}$$

V. RESULTS AND DISCUSSION

A. Jet path calculated from the electrically driven bending instability

We begin with the calculation of the development of the temporal perturbation into the bending instability. Figure 14 shows that the small perturbation, Eqs. (22), increased dramatically as the Earnshaw-like instability grew. The path of the electrified jet at $\bar{t}=0.89$ is represented by a helix of increasing radial dimension and a pitch commensurate with the radial dimension. It is emphasized that the jet at $\bar{t}=0$ would appear on the scale of Fig. 14 as a straight line, since the initial helix radius is very small in comparison to the other dimensions. As the calculation progresses, the beads move further and further apart. Since, in this model, the beads are connected by straight lines, the graph becomes quite irregular when the separation between the beads is larger than the radius of the spiral path.

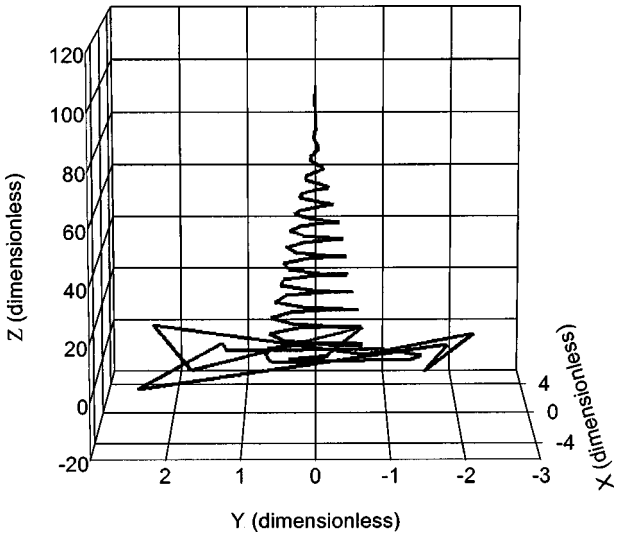

FIG. 14. Temporal growth of the bending instability along the straight segment of a charged jet subject to a small perturbation that is initially periodic in space. The growth of the lateral excursions is larger than that usually observed to show details of the model. The following values of the parameters were used: $Q=50$, $V=40$, $F_{ve}=50$, $A=0$, $K_t=1$, and $H=100$; $\bar{t}=0.89$. The number of beads $N=100$.

Consider now the development of perturbations into a bending instability in a realistic jet (spatial instability). We estimate the charge carried by the jet to be 1 C/l, which is of the same order as the values measured.[20] We also estimate that the relaxation time θ is 10 ms, a_0 is 150 μm, ρ is 10^3 kg/m^3, h is 2 m, V_0 is 10 kV, α is 0.7 kg/s^2, and μ is 10^3 kg/(m s). The value of μ is taken to be much larger than the zero-shear viscosity μ_0 reported,[20] since the strong longitudinal flows we are dealing with in the present work lead to an increase, by several orders of magnitude, of the elongational viscosity from μ_0.[9,22,27,28] The dimensionless parameters are as follows: $Q=F_{ve}=78359.6$, $V=156.7$, $A=17.19$, and $H=626.9$. The length scale is $L=3.19$ mm. The charge on the bead $e=8.48\,(\mathrm{g}^{1/2}\,\mathrm{cm}^{3/2})/\mathrm{s}=2.83\times10^{-9}$ C. The mass of each bead is $m=0.283\times10^{-8}$ kg. The value of K_s is taken as 100. Since $\theta=\mu/G=10$ ms, this value corresponds to $\omega=10^4\ \mathrm{s}^{-1}$, which is in the frequency range of typical noise in the laboratory.

Figures 15(a)–15(e) illustrate the development of a typical jet path. The time periodic perturbation, Eqs. (21), that grows along the jet is similar to the case shown in Fig. 14. The jet flows continuously from the pendent drop in response to the electric field established by the externally applied potential between the droplet and the collector. This electric field also causes the jet to be charged as it leaves the pendent drop. At $\bar{t}=0.99$ in Fig. 15(e) the instantaneous path of the jet is similar to the patterns recorded in experiments using a high speed video camera such as those shown in Fig. 2. It is emphasized that the stresses σ_{ui} and σ_{di} are positive along the entire jet in Figs. 15(a)–15(e), which means that the whole jet is stretched continuously.

In Fig. 15, a long segment near the vertex of the envelope cone is plotted in the x, y, and z coordinates at various times and scales to show details of the jet path. The entire length of both the straight segment and the spiral part is shown at the same scale in the inset at the upper right of each part of Fig. 15. An ellipse in each inset encloses the part of the jet path shown in the corresponding coordinate box. The pendent drop was always at $x=0$, $y=0$, and $z=h$.

The experimental evidence shows a self-similar, fractal-like process of development of the electrically driven bending instabilities. The diameter of the first generation of bending loops becomes larger and the jet becomes thinner. Then much smaller bending perturbations set in on these loops and begin to grow also. This self-similar process continues at smaller and smaller scales until viscoelastic force, surface tension or solidification of the jet arrest further bending. The numerical results in Fig. 15 describe only the emergence and growth of the first cycle of the loops. This is a consequence of the fact that the distances between the beads increase enormously in the simulation of the development of the first cycle. No new beads were added except at the top of the rectilinear segment. Therefore the capability of the present computer code to elucidate smaller details of the path decreases as the jet elongates enormously.

Figure 16 shows the path of a charged jet calculated from a realistic but different set of dimensionless parameters and perturbations than was used in Fig. 15. The path displays a bending instability generally similar to that shown in Fig. 15.

To show that the bending instability is driven by the Coulomb interaction, the charge, e, on the beads is taken to be zero so that $Q=0$. The electrical driving force for the bending instability is then zero, but the other parameters are exactly the same as those in Fig. 16. If a jet were then pulled downward by gravity, which can supply a downward component of force that acts on the segment in the same way as the downward component of the electrical force from the electrical field, one would expect the uncharged jet to be almost straight in spite of the small perturbations applied to it, since the perturbations would not develop into a bending instability. The calculated result with the same parameters as those in Fig. 16, but $Q=0$, is in fact a straight jet growing downward, even at a later time ($\bar{t}=8.99$). Increasing the ratio of the surface tension to the Coulomb force also stabilizes a charged jet. If A is increased to 9, by increasing the surface tension while all the other parameters are kept the same as those in Fig. 16 practically no bending occurs. The results for the gravity driven jet and for the high surface tension jet are not shown because the calculated jet path cannot be distinguished from a straight line at the scale in Fig. 16.

B. Measurements of the trajectory and velocity of a particular segment of a jet

Figure 17 is derived from measurements of a sequence of stereographic images of the part of a jet just below the apex of the envelope cone. The polyethylene oxide solution in water and ethanol that was used is the same as that used for Figs. 4 and 5. The exposure time was 0.25 ms. The po-

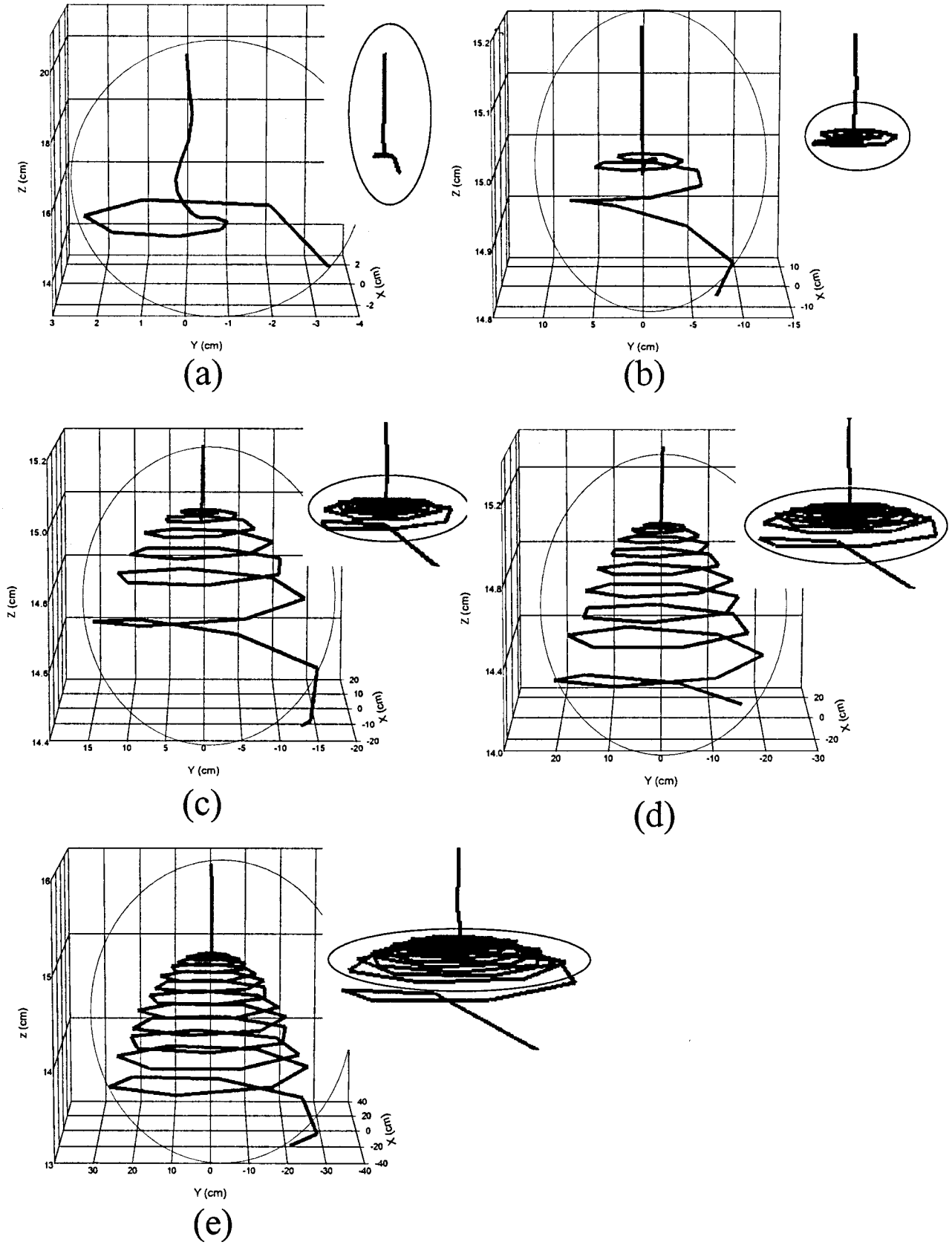

FIG. 15. Perturbations develop into a bending instability. The dimensionless groups have the following values: $Q=F_{ve}=78359.6$, $V=156.7$, $A=17.19$, $K_s=100$, $H=626.9$. (a) $\bar{t}=0.19$, (b) 0.39, (c) 0.59, (d) 0.79, and (e) 0.99.

sition projected into the plane of the image of the maximum lateral excursion of a loop, an example of which is marked with an arrow in Fig. 2, was followed as a function of time for 8 ms.

Figure 17 shows the downward displacement of the maximum lateral excursion from its initial position. The downward motion of the jet predicted by the model and the value measured from the experiment are of the same order of

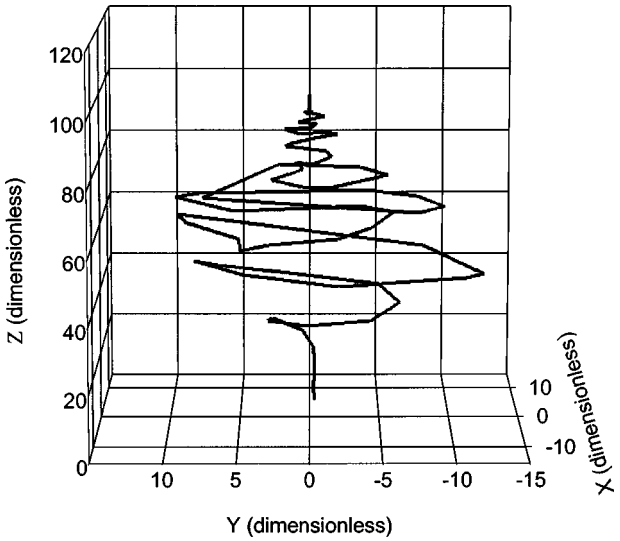

FIG. 16. Charged jet with values of the dimensionless parameters that are realistic but different from those used in Fig. 15. $Q=F_{ve}=12$, $V=2$, $A=0.9$, $K_s=100$, $H=100$, $\bar{t}=4.99$.

magnitude. Figure 18 shows the downward velocity, which decreased from about 1.1 to about 0.8 m/s. The increase in the radial displacement of the maximum is shown in Fig. 19. The measured radial velocity was nearly constant at a value of 0.5 m/s, as shown in Fig. 20.

The displacements of the maximum lateral excursion, given in Figs. 17 and 19, were fitted by the following expression, where z is measured from the pendent drop downward:

$$x=0.0257t^2\cos t,$$
$$y=0.0257t^2\sin t, \tag{25}$$
$$z=20\exp(-0.0595t).$$

Figure 21 is a three-dimensional plot of this equation. The position of ''maximum lateral excursion of a loop'' that was used as a reference to determine the velocities does not necessarily move in the same way as a marker embedded in the jet and carried with the jet. If a path with an elliptical loop were to rotate about its vertical axis, a changing segment of the jet would be projected into the image plane. The assumption that the velocity and displacement of the maximum lateral excursion represent the motion of a particular segment of the jet is essentially correct if the curve is not rotating, but only elongating along the axis of the segment, and moving radially outwards and downwards.

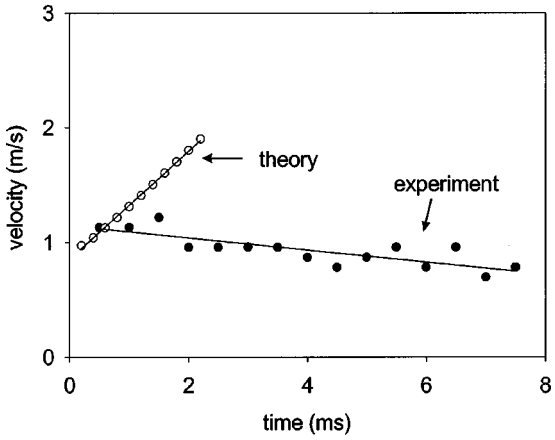

FIG. 18. Downward velocity of a maximum lateral displacement in a bending instability as a function of time.

The motion of a splay point such as that shown in Fig. 6, which is attached to a particular point on the jet, was observed in a series of stereo pictures. The motion of the splay point was only downward and outward in a plane that contained the y axis and a single radial direction, indicating that rotation of the path was small.

C. Bending instability leads to large area reduction ratios

The ''area reduction ratio,'' which is defined as the ratio of the cross-sectional area of the upper end of a segment to the cross-sectional area at the lower end of the same segment, is equal to the draw ratio if the volume of material in the segment is conserved. Since in this experiment the solvent evaporated during the process, the area reduction ratio was related to the draw ratio by the time varying concentration of the solution. Here we assume that the fluid jet was

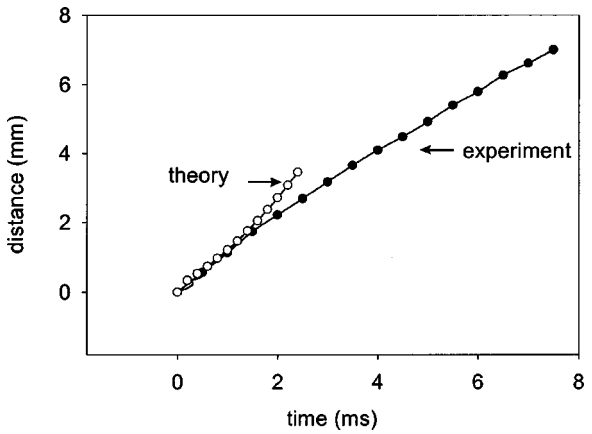

FIG. 17. Downward movement of a maximum lateral displacement in a bending instability as a function of time.

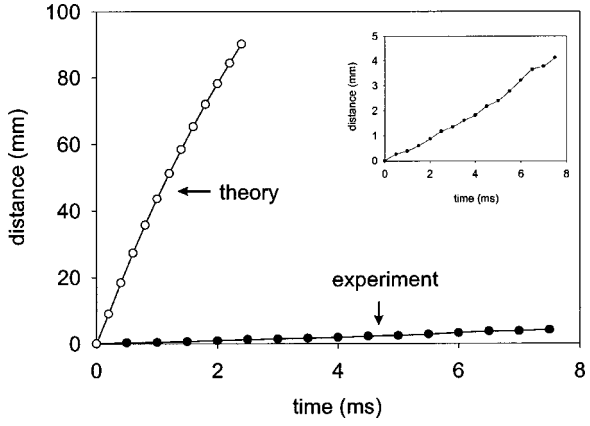

FIG. 19. Lateral movement of a maximum lateral displacement in a bending instability as a function of time. The inset shows the experimental results on an expanded distance scale.

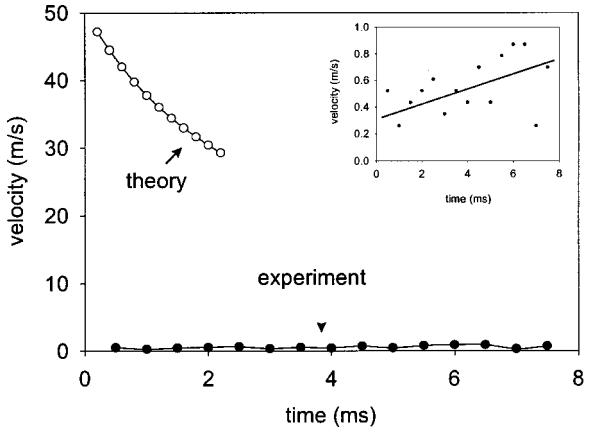

FIG. 20. Lateral velocity of a maximum lateral displacement in a bending instability as a function of time. The inset shows the experimental velocity on an expanded velocity scale.

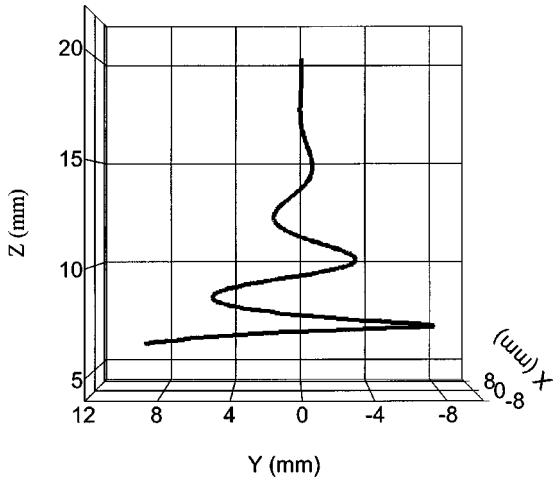

FIG. 21. Three-dimensional reconstruction of the bending jet.

drawn to a particular draw ratio and then the solvent was evaporated to produce a dry nanofiber with the observed diameter.

The examples that follow show that both the total area reduction ratio and the total draw ratio were large for a segment that contained the entire jet, starting at the surface of the droplet and ending in the dry nanofiber that was collected at the end of the process. For a jet that had a concentration of 6% polymer and a starting diameter of 100 μm, that produced a nanofiber with a diameter of 100 nm, the draw ratio not accounting for evaporation would be 10^6. The draw ratio of the jet accounting for evaporation is, however, $0.06 \times 10^6 = 60\,000$.

A draw ratio of 60 000 was routinely achieved in these experiments. Segments of the jet were drawn simultaneously in many expanding loops. If the jet were drawn in a straight line with a segment at the bottom end of the straight segment moving at a velocity of around 1.0 m/s, and then being elongated to a draw ratio of 60 000, the velocity achieved at the nanofiber end of the jet (about 60 000 m/s) would be 176 times faster than the speed of sound in air. The path actually observed achieves very high elongation without such an unreasonably high velocity by enlarging the diameters of many loops during the same time interval.

The calculation from the bending instability model supports the conclusion that, in the loops of the bending instability, the total draw ratio is very high. The initial distance between any two beads used in the calculation was $h/50\,000$, whereas the final distance between adjacent beads in the calculated loop, for example, in Fig. 15(e) is about $1.97h$. Assuming that the polymer concentration of the jet was 6%, the final cross-sectional radius of a dry fiber a_f, when all the solvent evaporates, is estimated as follows:

$$\pi a_f^2 \cdot 1.97h = \pi a_0^2 \frac{h}{50\,000} \cdot 0.06. \tag{26}$$

This yields $a_f \simeq 0.78 \times 10^{-3} a_0$. For $a_0 = 150\,\mu$m, we obtain $a_f \simeq 0.117\,\mu$m. This value is of the same order as those measured experimentally in Ref. 20, as well as those obtained in the experiment with $h = 0.2$ m. The corresponding draw ratio is 98 619. Also in the experiment, the bending instability occurs repeatedly at smaller and smaller scales, and the process becomes more and more fractal like, which is practically impossible to follow with numerical calculations of the sort used here. As a result, the total draw ratio and the total decrease in jet radius are both underestimated in the calculations.

D. Longitudinal strain rate and molecular orientation

The high value of the area reduction ratio and the associated high longitudinal strain rate imply that the macromolecules in the nanofibers should be stretched and axially oriented. Most electrospun nanofibers, even those made from a styrene-butadiene-styrene triblock copolymer, are birefringent.[29]

The longitudinal strain rate was different at different places along the jet. The longitudinal strain rate for three different parts of the jet was determined.

(1) The jet velocity in the downward direction was determined from the sequential images by determining the velocity of a particular maxima of the growing bending instability and the length of the straight segment. In this work, the length of the straight segment (L_z) was 5 cm and the velocity was 1 m/s. Therefore the longitudinal strain rate was ($\delta L_z / L_z \delta t$),

$$\delta L_z / L_z \delta t = V \delta t / L_z \delta t = V / L_z = (1\ \text{m/s}) \cdot (1/0.05\ \text{m}) = 20\ \text{s}^{-1}, \tag{27}$$

which is the rate of strain in the straight segment of the jet.

Warner *et al.*[17] measured the velocities along the straight segment with a laser Doppler velocimeter, and reported a velocity that increased from 1 to 15 m/s. Doppler velocimetry is most useful for monitoring the longitudinal strain rate, particularly where the jet diameter is large. The Doppler velocimetry data become more difficult to interpret when the bending instabilities are encountered.

(2) The observation of expanding loops provided a second measure of the longitudinal strain rate for the segment that formed the loop. A typical loop grew from a diameter of 1 to 8 mm in 7 ms. The resulting longitudinal strain rate in such a loop was $1000\ \text{s}^{-1}$.

(3) The overall longitudinal strain rate can be estimated using the data in Sec. V C. The time that a typical segment of the electrospun jet is in flight (δt) can be estimated as the distance between the pendent droplet and the collector (20 cm) divided by the average downward velocity of the jet (1 m/s). The resulting δt is 0.2 s. The longitudinal strain rate is $\delta\zeta/(\delta t \cdot \zeta)$, where ζ is the initial segment length, and $\delta\zeta$ is the growth in length. Since $\delta\zeta$ is much greater than ζ, $\delta\zeta$ is approximately the final segment length. The ratio $\delta\zeta/\zeta$ was around 10^5, and therefore the longitudinal strain rate was around $0.5\times10^6\ s^{-1}$. Using the estimate, Eq. (27), we find that in the straight segment the length of a liquid element has been approximately doubled, and the cross-sectional radius decreased by a factor of 4. Then the longitudinal strain rate in the loops becomes of the order of $10^5\ s^{-1}$. The actual value will be lower due to the effects of evaporation and solidification.

Theory suggests that the transformation from a random coil to a stretched macromolecule occurs when the strain rate multiplied by the conformational relaxation time of the molecule is greater than 0.5.[27,28] Since the relaxation time of this polymer solution is about 0.01 s, then $\delta\zeta/(\delta t \cdot \zeta)$ multiplied by the relaxation time was equal to $10-10^3$, which is much greater than 0.5. Therefore the longitudinal flow in the electrospun jet is strong, and the macromolecules are likely to be stretched in the direction of the jet axis.

VI. SUMMARY AND CONCLUSIONS

The initial straight segment of a typical electrically charged jet of polyethylene oxide aqueous solution was created by an electrical potential applied between the pendent drop and the collector. Then an electrically driven bending instability, triggered by perturbations of the lateral position and lateral velocity of the jet, grew. The repulsive forces between the charges carried with the jet caused every segment of the jet to lengthen continuously along a changing path until the jet solidified. The geometrically simple idea that the jet lengthened in a straight line along its axis leads to an implausibly high velocity at the thin, leading end of such a straight jet. Instead, the jet bent and developed a series of lateral excursions that grew into spiraling loops. Each of these loops grew larger in diameter as the jet grew longer and became thinner.

About 20 ms after a loop had first formed, occurring within a time interval of less than a millisecond, a new set of electrically driven bending instabilities appeared on the now thinner, smoothly curved loop. The new bending instabilities grew when the jet in the loop was thin enough and when the viscoelastic stress along its axis had relaxed enough. These new bending instabilities developed into a smaller set of spirals that looped around the path of the first loop.

The envelope cone observed at the end of the straight segment defined the region inside which this complex path of the jet developed. The cycles of bending instability repeated in a self-similar manner until the solvent evaporated, and the remaining polymer fiber resisted further elongation by the Coulomb forces of the charge that was still present on the jet. A very high reduction (as much as 10^5) in the cross-sectional area of the jet was achieved in this manner and the corresponding large increase in the jet length occurred in a region that was only a few centimeters across. The associated high longitudinal strain rate implies that, in the electrospun jet, the macromolecular coils are stretched along the axis of the jet.

Bending instabilities in electrospun jets were modeled by a system of connected viscoelastic dumbbells. Beads in the dumbbells possess appropriate mass and charge to represent the observed jets. The beads interacted with each other according to Coulomb's law. The beads were also subject to the electrical forces from the electrical field created between the pendent droplet and the collector by the imposed potential difference. Springs and dashpots, connecting the beads in the dumbbells, mimicked the Maxwellian viscoelastic resistance to elongation of the jet. Surface tension effects were also included. Estimates showed that effects of the Earth's gravity, as well as aerodynamic forces (the drag and distributed lift force), were negligibly small in the electrospinning experiments.

Equations of motion of the beads with all the forces acting in combination were used to follow, numerically, the evolution of the path of the electrically charged polymer jets in the presence of spatial and temporal perturbations. The results are in reasonable agreement with the experimental evidence. In spite of the fact that some material parameters can only be estimated at present, order of magnitude, or better, agreement between the theory and experimental observations was achieved. The theory showed that the viscoelastic force along the jet and the surface tension both tend to stabilize the charged jet.

The entire electrospinning process and the electrically driven bending instabilities of an electrospun fluid can each be viewed as particular examples of the very general Earnshaw theorem in electrostatics. This theorem leads to the conclusion that it is impossible to create a stable structure in which the elements of the structure interact only by Coulomb's law. Charges on or embedded in a polymer fluid move the fluid in quite complicated ways to reduce their Coulomb interaction energy. Electrospinning, and perhaps other useful processes, utilize this behavior to produce interesting and useful polymer objects.

For additional information on this topic, see Ref. 30.

ACKNOWLEDGMENTS

Support for this work was provided by the National Science Foundation under Grant Nos. DMI-9813098 and CTS-9900949, by the U.S. Army Research Office, by the U.S. Army Soldier and Biological Systems Command, and by the Nonmetallic Materials Division of the U.S. Air Force Research Laboratory, Wright Patterson Air Force Base. The high-speed camera was acquired with support from the Hayes Investment Fund of the Ohio Board of Regents. A gift from the DUPONT Company made it possible for Dr. Alex Yarin to make a productive visit to the University of Akron. The help of Dale Ertley and Dr. Dan Galehouse in the construction of many specialized pieces of equipment is greatly appreciated.

[1] X. Lord Rayleigh, London, Edinburgh, Dublin Philos. Mag. **44**, 184 (1882).
[2] J. Zeleny, Phys. Rev. **10**, 1 (1917).
[3] G. I. Taylor, Proc. R. Soc. London, Ser. A **280**, 383 (1964).
[4] G. I. Taylor, J. Fluid Mech. **22**, 1 (1965).
[5] G. I. Taylor, Proc. R. Soc. London, Ser. A **291**, 145 (1966).
[6] G. I. Taylor, Proc. R. Soc. London, Ser. A **313**, 453 (1969).
[7] A. L. Yarin, J. Appl. Mech. Tech. Phys. **23**, 39 (1982).
[8] A. L. Yarin, J. Appl. Mech. Tech. Phys. **27**, 828 (1986).
[9] A. L. Yarin, *Free Liquid Jets and Films: Hydrodynamics and Rheology* (Longman, Harlow, and Wiley, New York, 1993).
[10] V. M. Entov and A. L. Yarin, J. Fluid Mech. **140**, 91 (1984).
[11] P. K. Baumgarten, J. Colloid Interface Sci. **36**, 71 (1971).
[12] L. Larrondo, and R. St. J. Manley, J. Polym. Sci., Part B: Polym. Phys. **19**, 909 (1981).
[13] L. Larrondo and R. St. J. Manley, J. Polym. Sci., Part B: Polym. Phys. **19**, 921 (1981).
[14] L. Larrondo and R. St. J. Manley J. Polym. Sci., Part B: Polym. Phys. **19**, 933 (1981).
[15] D. H. Reneker and I. Chun, Nanotechnology **7**, 216 (1996).
[16] A. Formhals, U.S. Patent No. 1,975,504 (filed 1934).
[17] S. B. Warner, A. Buer, S. C. Ugbolue, B. C. Rutledge, and M. Y. Shin, National Textile Center Annual Report No. 83-90 (1998).
[18] A. G. Bailey, *Electrostatic Spraying of Liquid* (Wiley, New York, 1998), p. 21.
[19] J. S. Chang, A. J. Kelly, and J. M. Crowley, *Handbook of Electrostatic Processes* (Dekker, New York, 1995), p. 248.
[20] H. Fong, I. Chung, and D. H. Reneker, Polymer **40**, 4585 (1999).
[21] R. B. Bird, R. C. Armstrong, and O. Hassager, *Dynamics of Polymeric Liquids*, 2nd ed. (Wiley, New York, 1987), Vol. 1.
[22] A. L. Yarin, J. Non-Newtonian Fluid Mech. **37**, 113 (1990).
[23] R. W. Fox and A. T. McDonald, *Introduction to Fluid Mechanics*, 3rd ed. (Wiley, New York, 1985).
[24] D. V. Khakhar and J. M. Ottino, Int. J. Multiphase Flow **13**, 71 (1987).
[25] *High-Speed Fiber Spinning*, edited by A. Ziabicki and H. Kawai (Wiley, New York, 1985).
[26] J. Jeans, *The Mathematical Theory of Electricity and Magnetism* (Cambridge University Press, Cambridge, 1958).
[27] P. G. de Dennes, J. Chem. Phys. **60**, 5030 (1974).
[28] H. Chang and A. S. Lodge, Rheol. Acta **11**, 127 (1972).
[29] H. Fong and D. H. Reneker, J. Polym. Sci., Part B: Polym. Phys. **37**, 3488 (1999).
[30] See E-PAPS Document No. E-JAPIAU-87-O36009 for a film on bending instability (Bending-movie.avi). This document may be retreived via the E-PAPS homepage (http://www.aip.org/pubservs/epaps.html) or from ftp.aip.org in the directory/epaps/. See the E-PAPS homepage for more information.